CrossMark

Flow past a rotating cylinder translating at different gap heights along a wall

A. Rao [a,*], M.C. Thompson [a], T. Leweke [b], K. Hourigan [a]

[a] Fluids Laboratory for Aeronautical and Industrial Research (FLAIR), Department of Mechanical and Aerospace Engineering, 17 College Walk, Monash University, Clayton 3800, VIC, Australia
[b] Institut de Recherche sur les Phénomènes Hors Équilibre (IRPHÉ), UMR 7342, CNRS, Aix-Marseille Université, Centrale Marseille, 13384, Marseille, France

ARTICLE INFO

ABSTRACT

The flow past a rotating circular cylinder translating parallel to a wall at different heights is investigated for Reynolds numbers up to 400 for three discrete rotation rates. In particular, the various wake transitions that occur as a function of gap height are quantified for the three cases examined: non-rotation, and forward and reverse rotations. At low gap heights, only a single steady three-dimensional mode is found to become unstable on the steady base flow. As the gap height is increased, several new three-dimensional modes are observed, of which one attains large amplitudes in the near wake and another preferentially in the far wake. At still larger gap heights, the transition sequence resembles that observed in a rotating cylinder wake, for which the wake first undergoes transition to a periodic state, prior to the onset of three-dimensional flow. Parameter space maps showing the neutral stability curves and regions of instability for each mode are presented for each rotation rate, together with a discussion of the spatio-temporal characteristics and spatial distributions of the new modes. Finally, the force coefficients for the steady and periodic two-dimensional base flows are presented.

© 2015 Elsevier Ltd. All rights reserved.

1. Introduction

The wake of bluff bodies can be altered through external forcing, e.g., by induced rotation or oscillation, by introducing another bluff body in its vicinity or by changing physical boundaries. Here, a combination of two effects is studied: rotation and proximity to a surface. These effects have relevance to flows where wall-particle interactions are important. Examples include sedimentation tanks used in the chemical and mining industries, cells in blood vessels and micro-carrier beads in bioreactors (Gupta et al., 2014; Ismadi et al., 2014). Numerical modelling of bluff bodies would enable the prediction of the movement of these particles and their settling behaviour in the above stated applications.

Flow past isolated bluff bodies have been the subject of many investigations, and the nature of the wake has been explored in great detail. The experimental studies of Williamson (1988, 1996a,b) investigated the three-dimensional wake structures that evolve from a two-dimensional wake as the Reynolds number is increased. At approximately $Re = 190$ (with Re being the Reynolds number based on diameter), the previous two-dimensional wake vortices developed a strong waviness with a wavelength of approximately four cylinder diameters. This was termed *mode A* shedding. At higher Reynolds numbers ($Re \gtrsim 230$), a shorter wavelength mode (*mode B*) progressively dominated the wake. This had a spanwise wavelength of approximately one

---

* Corresponding author.
  E-mail address: anirudh.rao@monash.edu (A. Rao).

cylinder diameter. The instabilities responsible for these wake states were predicted by linear stability analysis (Barkley and Henderson, 1996), and also found in DNS (Direct Numerical Simulations) (Thompson et al., 1996, 2001; Henderson, 1997). The analogues of these modes were observed in the wakes of other bluff bodies, such as square cylinders (Robichaux et al., 1999) and elongated cylinders (Ryan et al., 2005). The periods of modes A and B correspond with those of the base flow. Modes that are incommensurate with the base flow have also been observed in bluff bodies wakes; such modes are known as quasi-periodic modes (Blackburn and Lopez, 2003; Blackburn et al., 2005). Subharmonic modes have also been observed when the wake symmetry is altered, as in the flow past rings (Sheard et al., 2005b, 2004a), and inclined square cylinders (Sheard et al., 2009; Sheard, 2011). In addition, such modes have also been observed in a non-rotating cylinder wake when a wire was placed downstream of the cylinder (Zhang et al., 2005; Yildirim et al., 2013) or upstream (Rao et al., 2015b).

The wake of a circular cylinder is substantially altered by applied rotation. An extra governing parameter that this introduces is the non-dimensional rotation rate, α, defined as the ratio of the cylinder surface speed to the relative freestream speed. As the rotation rate is increased from zero, the onset of unsteady flow is delayed to higher Reynolds numbers; for $\alpha \gtrsim 2$, vortex shedding was found to be suppressed for Re ≤ 400 (Mittal and Kumar, 2003; Kang et al., 1999; Akoury et al., 2008; Pralits et al., 2010; Rao et al., 2013a) until higher rotation rates, where it again reappears but only over a very small range of rotation rates Stojković et al., 2003, 2002; Mittal and Kumar, 2003). Recent linear stability analysis by Rao et al. (2013a,b) showed that the critical Reynolds numbers for the onset of modes A and B are increased as the rotation rate is increased from $\alpha = 0$. In fact, for rotation rates $1.5 \lesssim \alpha \lesssim 1.85$, a subharmonic mode, *mode C*, is the first three-dimensional mode to become unstable, prior to the onset of mode A. Two other modes having spatio-temporal characteristics similar to mode A were observed at higher rotation rates close to the boundary of transition to steady flow.

Placing a bluff body near a plane surface can alter the classical Bénard–von Kármán (BvK) shedding seen for isolated bluff bodies. The controlling parameter here is the gap ratio or more commonly the gap height (G/D), where the gap between the body (G) and wall is normalised by the cylinder diameter (D). For a circular cylinder at a gap height of $G/D = 0.1$, Taneda (1965) observed that the vortices were separated by large streamwise distances and diffused rapidly compared with those formed when the gap height was $G/D = 0.6$.

Huang and Sung (2007) investigated the flow past a non-rotating cylinder for Re < 600 and for $G/D \geq 0.1$. They observed that the critical gap height, below which alternate vortex shedding was suppressed, decreased from $G/D = 0.28$ to $G/D = 0.25$ as the Reynolds number was increased. They further quantified the forces on the cylinder and the non-dimensional shedding frequency or Strouhal number (St $= fD/U$, with f being the shedding frequency). For a given gap height, the shedding frequency was found to increase with Reynolds number. However, for a given Reynolds number, St increased over $0.15 < G/D < 0.5$ before decreasing at greater gap heights. Their numerical simulations were performed with the lower wall stationary. Similar investigations undertaken by Yoon et al. (2010, 2007), using an immersed-boundary method, quantified the forces on the cylinder for Re < 200. As the gap height was increased from low values, the drag and lift coefficients showed an exponential decrease. They further observed that the onset of unsteady flow was delayed to higher Reynolds numbers as the gap height was reduced. For $G/D = 0.1$, vortex shedding was first observed at Re $= 120$, as compared to Re $\simeq 47$ for a cylinder in freestream.

Recent investigations by Rao et al. (2013d) determined the variation of unsteady flow for a circular cylinder translating parallel to a wall for Re ≤ 200. They further quantified the forces and the shedding frequency with Reynolds number, as well as the onset of three-dimensional flow as the cylinder is moved from the freestream ($G/D = \infty$) towards the wall ($G/D = 0$). For gap heights $G/D \leq 0.25$, transition to three-dimensional flow occurred in the steady flow regime at low Reynolds numbers. They also tracked the onset of the mode A instability for $G/D \gtrsim 0.3$. While the spanwise wavelength at onset remained approximately $4D$, the critical Reynolds number decreased for $G/D \lesssim 0.45$ before increasing towards the freestream value of Re$_c \simeq 190$. Additionally, they demonstrated the occurrence of multiple instability modes in the wake at Re $= 200$, with interactions between these modes leading to a chaotic saturated wake state.

Very few studies have investigated the combination of rotation and wall proximity for bluff bodies. Russel et al. (1977) showed that long slender rods tend to rotate as they approached a wall, which was not the case in a symmetrical unbounded flow. More recently, Cheng and Luo (2007) investigated the flow for a rotating cylinder for $-1 \leq \alpha \leq +1$ at Re $= 200$ for a fixed lower wall. For low gap heights, the flow was observed to be steady, and on increasing the gap height, the flow became aperiodic, before the characteristic BvK street was observed at greater gap heights. The wake was displaced towards the wall for $\alpha < 0$ and away from it for $\alpha > 0$. They further quantified the lift and the drag forces experienced by the cylinder.

Stewart et al. (2006, 2010) investigated the flow past a rotating cylinder next to a wall. For rotation rates $-1 \leq \alpha \leq +1$, the experimental and numerical investigations showed significant differences in wake structures compared with those for bodies in freestream. In addition, the onset of unsteady flow occurred at higher Reynolds numbers compared with bodies in freestream. As the rotation rate was decreased, the onset of unsteady flow increased to higher Reynolds numbers. Furthermore, linear stability analysis showed that the onset of three-dimensional flow occurred prior to the wake becoming (two-dimensionally) unstable. Their numerical and experimental investigations were in good agreement. That study was extended by Rao et al. (2011) with the rotation rate range expanded to $-2 \leq \alpha \leq +2$. For $\alpha \leq -1.5$, vortex shedding was suppressed and for $\alpha \leq -2$, the flow remained two-dimensional for Re ≤ 750. For forward rolling cylinders, the onset of both three-dimensional and unsteady flow occurred at very low Reynolds numbers (Re $\lesssim 50$).

In this study, we characterise the wake transitions of a translating, rotating circular cylinder, positioned at different heights from a stationary wall in a quiescent fluid. The parameter space considered covers gap heights from almost touching the wall ($G/D \simeq 0$) to freestream ($G/D \rightarrow \infty$), for Re ≤ 400 and three rotation rates $\alpha \in (+1, 0, -1)$. Characteristics of the
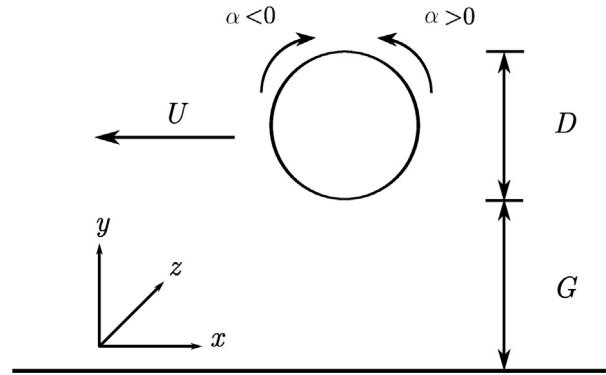
Fig. 1. Schematic of the problem. The cylinder of diameter D is translating with velocity U, above the wall at height G. The cylinder rotation rate, α is set to $+1, 0$ and -1, where positive value indicates anticlockwise rotation and negative value indicates clockwise rotation.

two-dimensional base flows are presented first, followed by linear stability analysis of these wakes. The various three-dimensional transitions are examined as a function of gap height, followed by a discussion of some targeted three-dimensional simulations to explore the saturated wake states.

2. Numerical method

2.1. Problem setup and parameter definition

The schematic of the problem under investigation is shown in Fig. 1. The cylinder of diameter (D) translates parallel to a solid wall at speed (U), and has a fixed rotation rate (α), defined as the ratio of the cylinder surface speed to the translational speed. The height of the cylinder above the wall (G) is non-dimensionalised by the cylinder diameter to obtain the gap ratio or gap height (G/D). The final governing parameter is the Reynolds number $\text{Re} = UD/\nu$, where ρ and ν are the density and kinematic viscosity of the fluid, respectively.

In this study, the rotation rate is set to $\alpha = +1$ (anticlockwise rotation) or -1 (clockwise rotation), with non-rotation ($\alpha = 0$) providing the benchmark case for comparison. The gap height is varied between $G/D = 0.005$ (near wall) and ∞ (freestream), and the maximum Reynolds number considered is $\text{Re} = 400$.

2.2. Numerical formulation

To obtain the base flow, the incompressible Navier–Stokes (NS) equations were solved in two dimensions using a spectral-element formulation. The computational domain consisted of several hundred quadrilateral macro-elements, with higher concentration in the vicinity of the rotating cylinder where the velocity gradients were largest. These elements were further subdivided into internal node points (N) distributed according to Gauss–Legendre–Lobatto quadrature points in two dimensions. The velocity and pressure fields were represented by tensor products of Lagrangian polynomial interpolants. This method achieves spectral convergence as the polynomial order is increased within elements (Karniadakis and Sherwin, 2005). The number of node points within each element ($N \times N$) is specified at runtime, with the interpolating polynomial order in each direction being $N - 1$. A second-order fractional time-stepping technique was used to sequentially integrate the advection, pressure and diffusion terms of the Navier–Stokes equations forward in time. The unsteady solver was used to investigate the parameter range covering both the steady and unsteady regimes of flow. More details of the time-stepping scheme can be found in Thompson et al. (2006a), and the code has previously been used to accurately compute bluff body flows in freestream (Sheard et al., 2004b; Ryan et al., 2005; Leontini et al., 2007; Rao et al., 2013a; Thompson et al., 2014), and for bodies near walls (Stewart et al., 2006, 2010; Rao et al., 2011, 2013d, 2012).

The computational domain size was adjusted such that critical values, such as force coefficients and shedding frequencies, were insensitive to placing the boundaries further away, generally to better than 1%. The cylinder was positioned centrally within the boundaries located 100D away from the cylinder, in line with previous studies (Stewart et al., 2010; Rao et al., 2013c), for which full domain size and resolution studies were undertaken.

2.3. Linear stability analysis

Linear stability analysis is widely used to understand the transitions occurring in bluff body wakes as the control parameters are varied. For an isolated circular cylinder, Barkley and Henderson (1996) used this technique to predict the onset of mode A and B instabilities along with their spanwise wavelength, and those predictions were in excellent agreement with the findings from experimental studies of Williamson (1996b). To determine the linear stability to three-dimensional transition, the Navier–Stokes equations are linearised about a periodic or steady base flow state, with the

spanwise variation of the perturbation variables constructed as a set of Fourier terms. To examine three-dimensional transition, for a selected spanwise wavelength, these equations are integrated forward in time from a white noise initial state and the growth of perturbations is monitored. After several wake periods, the fastest growing modes dominate. For a periodic base flow, the amplification of these dominant modes is determined over each base flow period; this technique is known as Floquet analysis. If the base flow is steady, it is convenient to measure the growth rate over a unit time. In both cases, the stability multiplier (μ) measures the amplification rate of the perturbations over the chosen time interval (T). This is called the Floquet multiplier for the periodic base flow case. In either case, the growth rate (σ) is determined by $\sigma = \ln(\mu)/T$. For growth rates greater than 0 (or $|\mu| > 1$), the flow is unstable to three-dimensional perturbations at the chosen wavelength and for $\sigma < 0$ (or $|\mu| < 1$), perturbations decay and the flow remains in its two-dimensional state. For $\sigma = 0$ (or $|\mu| = 1$), neutral stability is achieved. For a given Reynolds number, a range of spanwise wavelengths are tested, and this procedure is repeated for a range of Reynolds numbers to determine the critical Reynolds number and wavelength at which neutral stability is achieved. For the transition from two-dimensional steady to two-dimensional periodic flow, the method can also be applied by considering a spanwise wavelength approaching infinity. The complex growth rate or multiplier then gives the growth rate and frequency of the unstable oscillatory mode. In order to determine the boundary of transition of a three-dimensional mode, this procedure is repeated over a range of gap heights.

For the classical case of the circular cylinder wake, modes A and B have real Floquet multipliers, implying that these modes are periodic with the same period as the base flow (Barkley and Henderson, 1996). However, three-dimensional modes exist which are incommensurate with the base flow and are termed quasi-periodic modes. Those modes have complex Floquet multipliers. This type of instability mode exists for a circular cylinder (Blackburn and Lopez, 2003; Blackburn et al., 2005) and a square cylinder in freestream (Robichaux et al., 1999). Another type of mode, which has a periodicity of $2T$ (i.e., it is subharmonic), has been found in wakes behind tori (Sheard et al., 2005a; Thompson et al., 2006b), inclined square cylinders (Sheard, 2011; Sheard et al., 2009), and in rotating cylinders (Rao et al., 2013a, 2014). The description here is brief and more details can be found in, e.g., Ryan et al. (2005), Leontini et al. (2007, 2013), and Rao et al. (2015a).

2.4. Resolution studies

The numerical setup uses a frame-of-reference with its origin at the centre of the cylinder. In this frame, the cylinder is stationary and there is a uniform fluid flow of speed U to the right. This velocity is assigned to the top and bottom boundaries, in addition to the domain inlet. The top, inlet and the outlet boundaries are placed $100D$ from the centre of the cylinder to prevent significant blockage, as has been done with previous studies (Stewart et al., 2010; Rao et al., 2011, 2015a). The computational domains consist of hundreds of quadrilateral macro-elements, which are internally subdivided. The number of node points per quadrilateral element ($N \times N$) can be varied at runtime, thereby allowing one mesh to be used for resolution tests. The number of internal node points was varied between $N^2 = 16$ and $N^2 = 121$. A new computational mesh was required for each gap ratio, although the concentration of mesh points in the neighbourhood of the cylinder, and more generally within the computational domain, was consistent between meshes. Resolution tests were carried out on a representative sample of these meshes to ensure the predicted flows were fully resolved. Spatial resolution studies were conducted at $G/D = 0.01, 0.1, 0.2, 0.5, 1, 2.5$, and 5 for the three rotation rates ($\alpha = -1, 0$ and $+1$); at the maximum Reynolds number studied (Re=400). For all cases, a resolution of $N^2 = 81$ was found to be sufficient to capture the time-averaged force coefficients and shedding frequencies (St) to well within 0.5% of those using the maximum tested resolution at $N^2 = 121$. Since the instability modes may have finer-scale structures than those of the base flow vortices, further resolution checks were also undertaken as part of the stability investigations to ensure that the Floquet multipliers/growth rates were adequately resolved. It was found that the resolution was also adequate to accurately resolve the instability modes.

3. Results

The parameter space investigated covered cases for bodies at gap heights of $G/D \simeq 0$ to ∞, Re ≤ 400 and for rotation rates of $\alpha \in \{+1, 0, -1\}$. For each of the three rotation rates, the stability of the flow in the Re–G/D parameter space is first presented, followed by the discussion of the various transitions that take place. The parameter maps show the marginal stability curves for the dominant modes for both steady and unsteady base flows. To create these maps, two-dimensional base flows were initially computed for each Reynolds number and gap height. Subsequently, linear stability analysis of these base states was undertaken to obtain the (complex) growth rates, generally for a wide range of spanwise wavelengths. Instability modes could be identified corresponding to ranges of spanwise wavelength. These data could then be used to construct functional fits through the growth rate maxima to give the preferred wavelength and growth rate of each mode, corresponding to a particular Reynolds number/gap height combination. To predict the neutral stability curves often required further simulations and stability analyses to refine the critical Reynolds numbers for each gap height. This is an expensive procedure; the cumulative computational runtime for these simulations was in excess of 10^5 CPU hours.

3.1. Pure translation: $\alpha = 0$

Flow past a non-rotating translating cylinder at different heights above a wall was investigated by Rao et al. (2013d), where it was observed that the transition to three-dimensional flow occurred from a steady base flow at low gap heights.

Furthermore, for larger gaps ($0.3 \leq G/D \leq 4$) for which three-dimensional transition occurs from a periodic base flow, the critical Reynolds number for mode A transition was mapped for Re ≤ 200. In this study, we extend the range of Reynolds number up to 300 to track the transition of three-dimensional modes whose wavelengths differ from mode A. The parameter space map is presented in Fig. 2(a), with an enlarged view in Fig. 2(b). On the steady state, mode E is the first three-dimensional mode to become unstable to spanwise perturbations for $G/D \lesssim 0.22$, as Reynolds number is increased. As the gap height is increased, new three-dimensional modes develop on the unsteady base flow, with high growth rates in the elongated shear layers. For $G/D \gtrsim 0.25$, mode A is the first mode to become unstable, and for $G/D \gtrsim 1$, mode B becomes unstable at or below Re=300. For $G/D \gtrsim 2$, the critical Reynolds numbers for these transitions quickly asymptote to the values observed for an isolated non-rotating cylinder.

3.1.1. Two-dimensional flow

For the cylinder translating near a wall, the flow structures and shedding frequencies have been reported in Rao et al. (2013d) for Re ≤ 200. The flow structures are not significantly different to those visualised in Rao et al. (2013d). On increasing the Reynolds number, the Strouhal number increases monotonically for a particular gap height. Fig. 3 shows the variation of Strouhal number with gap height for Re ≤ 300, where it is observed that for any given Reynolds number, Strouhal number increases slightly as the gap is decreased, followed by a sharp decrease as the gap approaches zero.

3.1.2. Three-dimensional flow

This section extends the investigation of Rao et al. (2013d) to Re=300, where two new three-dimensional modes have been identified along with the mapping of the unstable region of mode B instability. For gap heights $G/D \lesssim 0.22$, mode E is the first three-dimensional mode to become unstable and this occurs for a steady base flow. While this mode was previously observed in the studies of rotating cylinders near a wall (Stewart et al., 2010; Rao et al., 2011, 2013d; Hourigan et al., 2013), the nomenclature used here is borrowed from studies of an isolated rotating cylinder (Rao et al., 2013a,b, 2015a; Radi et al., 2013), given the perturbation field of mode E from those studies bears a strong similarity (also see section 3.6, Figs. 6 and 7 of Rao et al., 2013d). The stability multiplier of this mode is purely real and positive, and the critical spanwise wavelength at onset increases as the gap height is increased. For a cylinder translating along a wall, the growth rate of mode E increases to higher values as the Reynolds number is increased. Multiple three-dimensional modes are observed once the base flow becomes unsteady. Three-dimensional direct numerical simulations (DNS) at Re=200 for a cylinder sliding along a wall
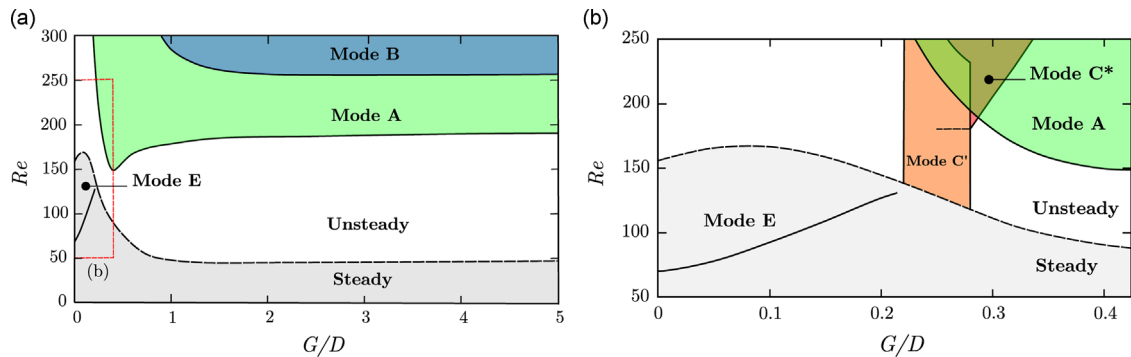

Fig. 2. (a) Parameter space for the non-rotating cylinder, i.e., at $\alpha = 0$, showing the regimes of steady and unsteady flows and the existence of the various three-dimensional modes for $G/D \leq 5$, Re ≤ 300. The black dashed line (- -) indicates the approximate boundary of the transition to unsteady flow. (b) Enlarged view of (a), showing the mode C′ and C* transitions that occur for $G/D \leq 0.45$.
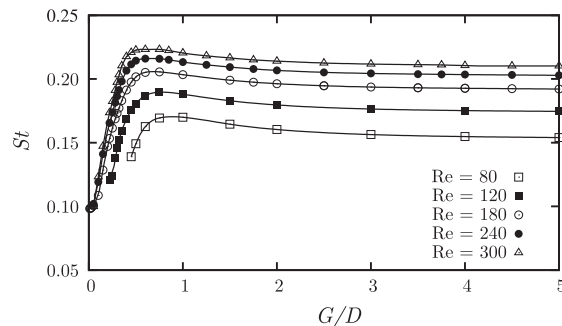

Fig. 3. Variation of St with G/D for the non-rotating cylinder at the specified Reynolds numbers.

show that the three-dimensional periodic flow eventually undergoes transition to a chaotic state (Rao et al., 2013d).

For gap heights $0.25 \lesssim G/D \lesssim 0.35$, two new three-dimensional modes are observed, both of which are subharmonic in nature. The first of these modes occurs near the boundary of transition to unsteady flow for $0.25 \lesssim G/D \lesssim 0.28$. The perturbation grows in the stretching shear layers between the forming vortex and the weaker vortices forming at the side of the cylinder closer to the wall, leading to high amplification rates. The Floquet multiplier is purely real and negative, and this mode is named mode C′. Shown in Fig. 4 are the spanwise perturbation vorticity contours of mode C′ at two gap heights. Fig. 4(c) and (d) shows the three-dimensional reconstruction of this mode in perspective and plan views, respectively.

For $0.28 \lesssim G/D \lesssim 0.35$, $\mathrm{Re} \simeq 180$, a second subharmonic mode is observed for $\lambda/D \simeq 2$. While this mode has its genesis in mode C′, a clear bifurcation of the two modes is seen. The perturbations of this subharmonic mode grow into a far wake, for downstream distances $\gtrsim 20D$, before dissipating further downstream. To distinguish this mode from mode C′, it is named C*. Shown in Fig. 5 are the perturbation vorticity contours of the mode C* instability. The perturbations grow when the vortices shed from the cylinder rearrange to form two vortex rows downstream of the cylinder. The spanwise wavelength of this mode is marginally larger than mode C′. Fig. 5(c) and (d) shows the three-dimensional reconstruction of this mode in terms of perturbation spanwise vorticity, in perspective and plan views, respectively.

As the gap height is increased beyond $G/D \gtrsim 0.4$, the transition to three-dimensionality is similar to that for the isolated non-rotating cylinder, with the transition to mode A followed by mode B at a higher Reynolds number. The variation of the transition to mode A with gap height was previously documented in Rao et al. (2013d) for $G/D \leq 0.28$, $\mathrm{Re} \leq 200$. Mode A persists at higher Reynolds numbers with a higher growth rate. The transition to mode B is found at decreasing Reynolds numbers as the gap height is increased. The critical wavelength at the onset of mode B increases from $\lambda_c/D = 0.74$ at $G/D = 1$ to $\lambda_c/D = 0.82$ at $G/D = 5$. Shown in Fig. 6(a) and (c) are the spanwise perturbation vorticity contours for mode A at $G/D = 0.25$ and $G/D = 5$, while Fig. 6(b) and (d) show the spanwise perturbation vorticity contours for mode B at $G/D = 1$ and $G/D = 5$. The three-dimensional reconstruction of modes A and B has previously been shown in Barkley and Henderson (1996), Robichaux et al. (1999), Rao et al. (2013a).

Table 1 summarises the various three-dimensional modes observed in the wake of a non-rotating cylinder translating along a wall. The characteristic wavelength of the modes, the two-dimensional base flow on which they occur, the nature of the stability/Floquet multiplier and the approximate gap height at which they occur are tabulated.
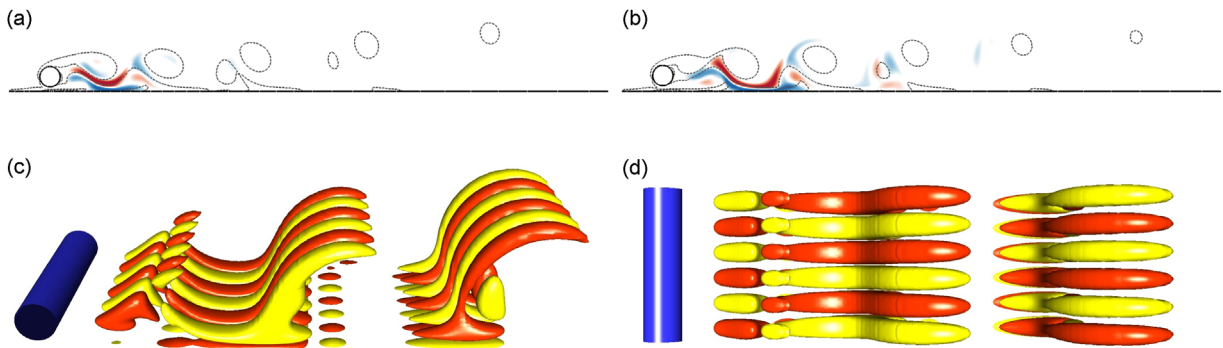

Fig. 4. Visualisation of the spanwise perturbation vorticity contours for the mode C′ instability at the specified gap heights, Reynolds number and spanwise wavelength for the non-rotating cylinder. Spanwise perturbation vorticity contour levels are between $\pm 0.1D/U$ and are overlaid by dashed lines (- -) which indicate the base flow vorticity contour levels between $\pm 1D/U$. (c) and (d) Three-dimensional reconstruction of this mode at $G/D = 0.28$, $\mathrm{Re} = 135$, $\lambda/D = 1.35$, visualised over a spanwise distance of $z/D = 4.05$, in perspective and plan view, respectively, showing three wavelengths of this instability. Isosurfaces of streamwise perturbation vorticity (in red and yellow) are visualised with the translating cylinder (in blue). Flow is from left to right in all images (a) G/D = 0.22, Re = 150, λ/D = 1.4 and (b) G/D = 0.28, Re = 135, λ/D = 1.35. (For interpretation of the references to colour in figure captions of this article, the reader is referred to the web version of this paper.)
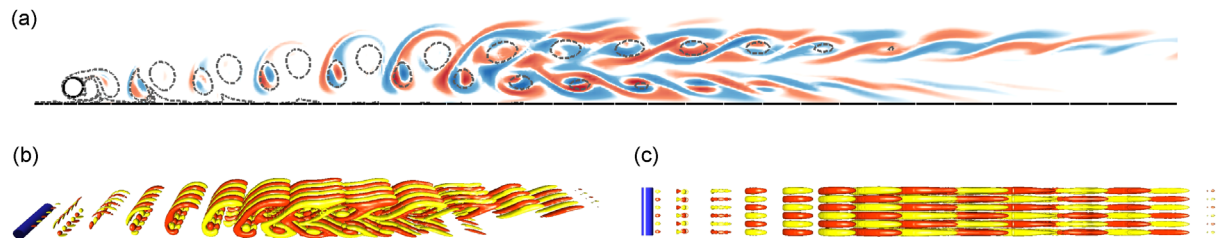

Fig. 5. (a) Visualisation of the spanwise perturbation vorticity contours for the mode C* instability at the specified gap heights, Reynolds number and spanwise wavelength for the non-rotating cylinder. The wake is visualised for a streamwise distance of $\gtrsim 55D$. Contour shading as per Fig. 4. The perturbation field clearly switches every alternate vortex, demonstrating the subharmonic nature of this mode. (b) and (c) Three-dimensional reconstruction of this mode visualised over a spanwise distance of $z/D = 4.5$, in perspective and top view, respectively, showing three wavelengths of this instability. Flow is from left to right in all images (a) G/D = 0.35, Re = 280, λ/D = 1.5.

3.2. Translation plus forward rolling: $\alpha = +1$

Fig. 7 shows the transition parameter map for a cylinder translating parallel to a wall as a function of gap height and Reynolds number, for a rotation rate of $\alpha = +1$. For the forward rotation case, the parameter space is covered for $G/D \le 5$ and Re ≤ 350. Previous investigations for a circular cylinder translating along a wall showed that the transition to three dimensionality occurred on a steady base flow (Stewart et al., 2010; Rao et al., 2011), while for the rotating cylinder in freestream at $\alpha = 1$, the transition to mode A occurred at Re$_c \simeq 270$, with a second three-dimensional transition to mode B occurring at a higher Reynolds number of Re $\simeq 350$ (Akoury, 2008; Rao, 2013a). The steady three-dimensional mode at small gap heights first observed by Stewart et al. (2010) and in subsequent studies (Rao et al., 2011, 2013d) is also predicted here. Two new three-dimensional modes were observed on the unsteady base flow, apart from modified forms of the well-known instabilities corresponding to modes A, B, C and QP, which have previously been observed in bluff body wakes (Barkley and Henderson, 1996; Robichaux et al., 1999; Blackburn et al., 2005; Blackburn and Lopez, 2003; Sheard et al., 2005a).
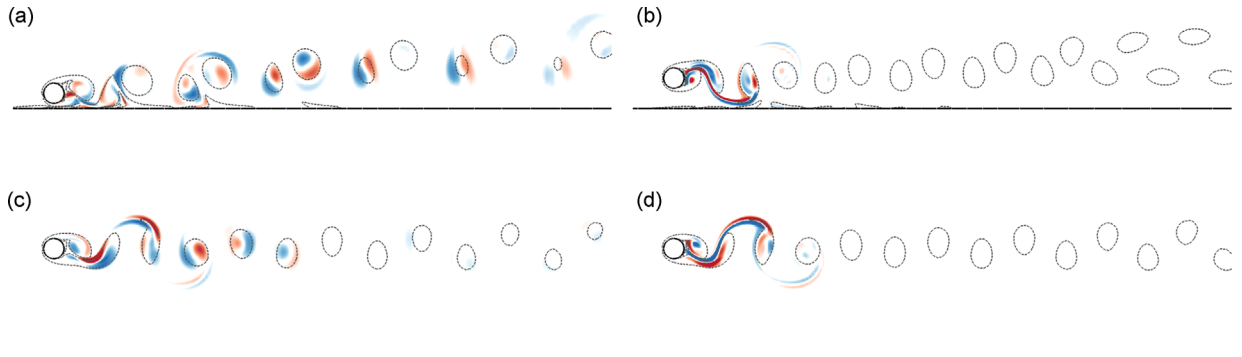

Fig. 6. Visualisation of the spanwise perturbation vorticity contours for the mode A (subfigures (a) and (c)) and mode B instability (subfigures (b) and (d)) at the specified gap heights, Reynolds number and spanwise wavelength for the non-rotating cylinder. Contour shading as per Fig. 4. Flow is from left to right in all images (a) mode A: $G/D = 0.25$, Re $= 240$, $\lambda/D = 4.25$, (b) mode B: $G/D = 1$, Re $= 300$, $\lambda/D = 0.75$, (c) mode A: $G/D = 5$, Re $= 200$, $\lambda/D = 3.75$ and (d) mode B: $G/D = 5$, Re $= 260$, $\lambda/D = 0.82$.

Table 1
Summary of the modes showing the approximate characteristic wavelength, nature of the Floquet multiplier (μ), gap height at which the instability occurs and the base flow on which the mode occurs for the non-rotating cylinder for Re ≤ 300.

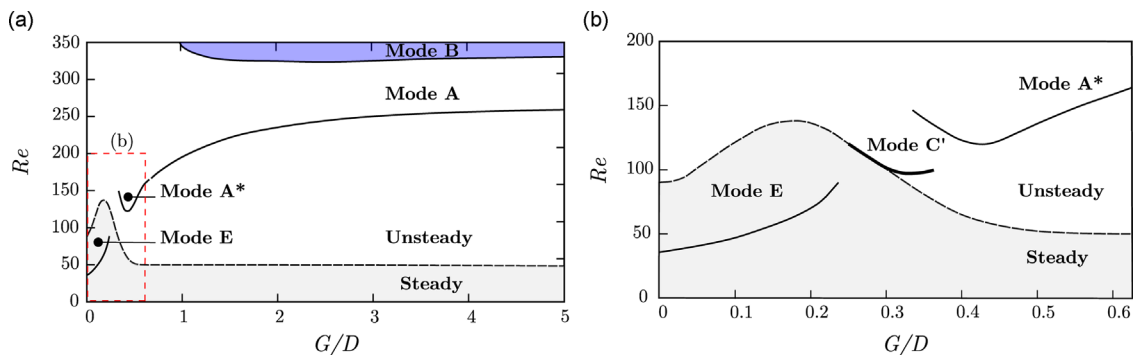| Mode	λ/D	Base flow	Nature of μ	Gap height
A	$\simeq 4$	Unsteady	Periodic	$\gtrsim 0.25D$–∞
B	$\simeq 0.8$	Unsteady	Periodic	$\gtrsim 0.85D$–∞
C'	$\simeq 1.25$	Unsteady	Subharmonic	$\simeq 0.22D$–$0.28D$
C*	$\simeq 1.5$	Unsteady	Subharmonic	$\simeq 0.28D$–$0.35D$
E	$\simeq 6$	Steady	Linear growth	0–$0.2D$

Fig. 7. (a) Parameter space for the cylinder rotating at $\alpha = +1$ showing the regimes of steady and unsteady flows and the existence of the various three-dimensional modes for $G/D \le 5$, Re ≤ 350. (b) Enlarged area of (a) showing the transitions that occur for $G/D \lesssim 0.6$, Re ≤ 200. The onset of mode C' occurs just after the transition to unsteady flow. The steady regions of flow are shaded in grey and the dashed line (- -) indicates the approximate Reynolds number for the transition from steady to unsteady flow in both diagrams.

3.2.1. Two-dimensional flow

3.2.1.1. Variation of force coefficients. Figs. 8 and 9 show the variation of the force coefficients with Reynolds numbers for the steady and unsteady regimes from two-dimensional simulations, respectively. These curves are similar to, but extend, those reported in the studies by Stewart et al. (2010) and Rao et al. (2013d) for cylinders at small gap heights. On the steady flow, the drag and lift force coefficients decrease with increasing Reynolds number. The variation of the time-averaged drag coefficient on the steady base flow takes the form $\overline{C_d} = a(\mathrm{Re})^b(G/D)^c$; where, $a \simeq 10.88$, $b \simeq -0.45$ and $c \simeq -0.18$. On the unsteady flow, the variation of the coefficients with Reynolds number is large for low gap heights compared with the higher gap height cases. It should be remembered that the flow becomes three-dimensional on the steady flow prior to becoming unsteady at low gap heights and thus these predictions may not be truly representative of those for fully three-dimensional flow.

Fig. 10 shows the variation of the Strouhal number with gap height for forward rotation for $G/D \geq 0.35$. The trends are similar to the $\alpha = 0$ case with St increasing with Re for a given gap height. The gap height at which the maximum Strouhal number occurs decreases as the Reynolds number is increased.

3.2.2. Three-dimensional flow

3.2.2.1. Mode E. Similar to the non-rotating cylinder case, mode E becomes unstable on the steady base flow for the cylinder translating with a rotation rate of $\alpha = 1$. The stability multiplier for this mode is again real and positive, and the critical Reynolds number and spanwise wavelength at onset increases monotonically with gap height. Fig. 11 shows spanwise perturbation vorticity contours for specified gap heights and Reynolds numbers. The perturbations grow in the elongated shear layers in the near wake. Fig. 11(c) and (d) shows three-dimensional reconstructions of this mode in perspective and plan views, respectively.

At higher Reynolds numbers, the growth rate of this mode increases, accompanied by an increase in the spanwise wavelength at which the maximum growth occurs. For a non-rotating cylinder translating along a wall, Rao et al. (2013d) showed that multiple modes become unstable on the unsteady wake, and the possible interaction of these modes leads the flow to a chaotic state. It is highly plausible that a similar situation could arise for the forward-rolling cylinder at a much lower rotation rate.

3.2.2.2. Mode C′. For $0.25 \leq G/D \lesssim 0.4$, the two-dimensional base flow becomes unstable to a subharmonic mode, mode C′ similar to the situation for a non-rotating cylinder. The critical Reynolds number for this mode decreases from Re $\simeq 120$ to
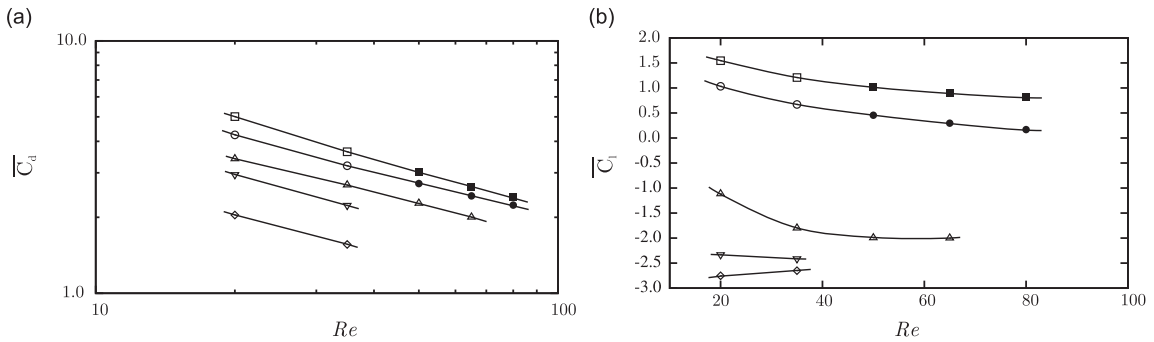

Fig. 8. Variation of the time-averaged drag and lift coefficient with Re from two-dimensional simulations, for various gap heights for the cylinder translating with a rotation rate of $\alpha = +1$ in the steady regime Re ≤ 100. Open symbols indicate the flow is two-dimensional, while filled symbols indicate the flow is three-dimensional. Legend: square ($\square$, $\blacksquare$) - $G/D = 0.05$; circle ($\circ$, $\bullet$) - $G/D = 0.1$; upright triangle ($\triangle$, $\blacktriangle$) - $G/D = 0.4$; inverted triangle ($\triangledown$, $\blacktriangledown$) - $G/D = 0.75$; diamond ($\diamond$, $\blacklozenge$) - $G/D = 4$.
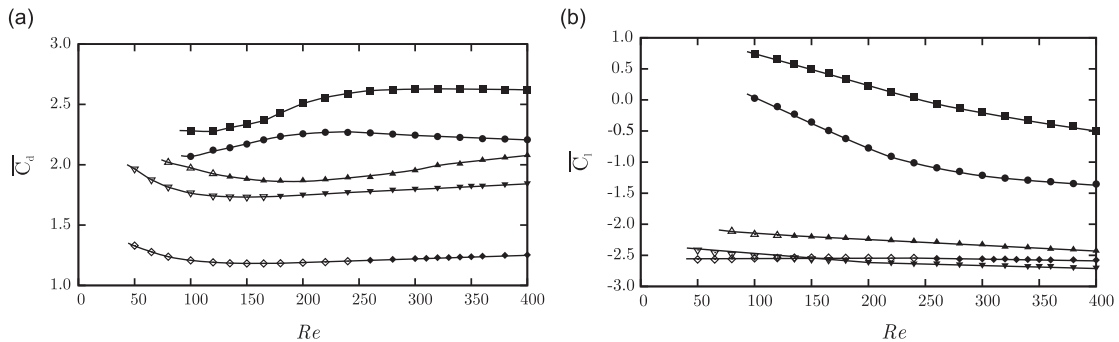

Fig. 9. Variation of the time-averaged drag and lift coefficient with Re, for various gap heights for the cylinder translating with a rotation rate of $\alpha = +1$ in the unsteady regime Re ≤ 400. Open symbols indicate the flow is two-dimensional, while filled symbols indicate the flow is three-dimensional. Legend: square ($\square$, $\blacksquare$) - $G/D = 0.05$; circle ($\circ$, $\bullet$) - $G/D = 0.1$; upright triangle ($\triangle$, $\blacktriangle$) - $G/D = 0.4$; inverted triangle ($\triangledown$, $\blacktriangledown$) - $G/D = 0.75$; diamond ($\diamond$, $\blacklozenge$) - $G/D = 4$.
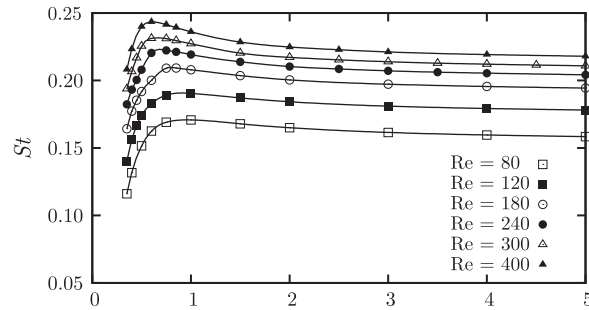
Fig. 10. Variation of St with G/D for the forward rolling cylinder ($\alpha = +1$) at the specified Reynolds numbers.
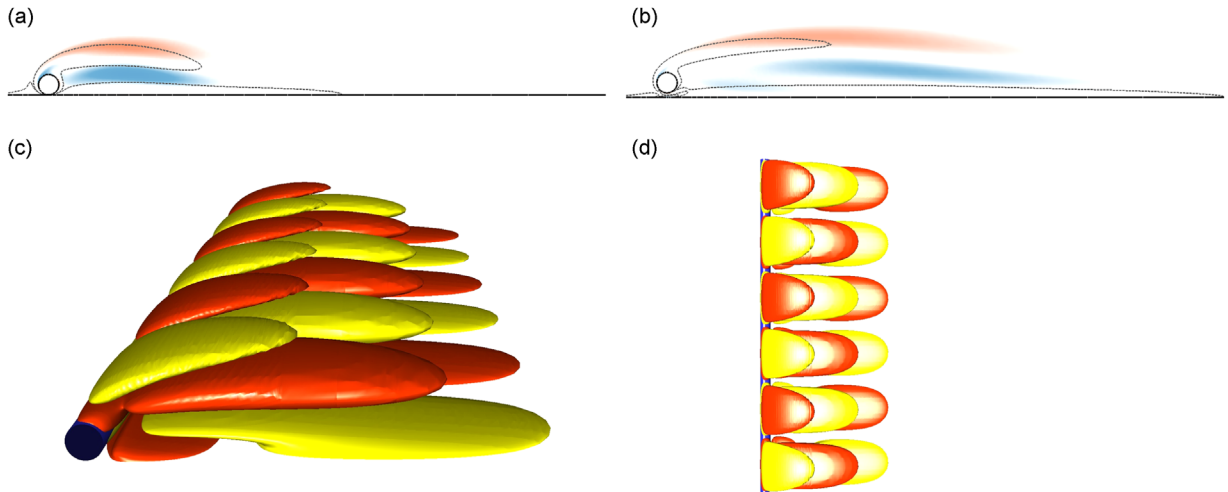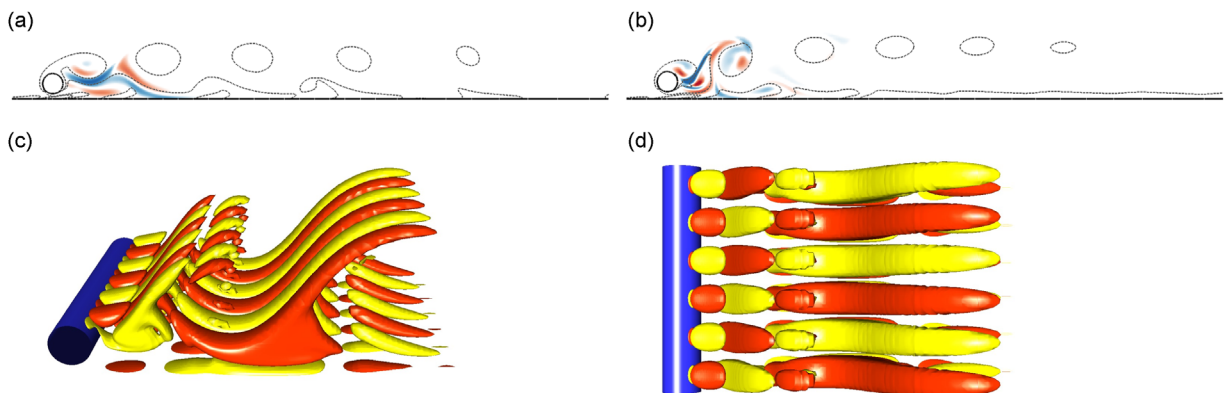

Fig. 11. (a) and (b) Visualisation of the spanwise perturbation vorticity contours for the mode E instability for the rotating cylinder at $\alpha = +1$ at the specified parameter values. Contour shading as per Fig. 4. (c) and (d) Three-dimensional reconstruction of this mode at $G/D = 0.1$, Re = 50, $\lambda/D = 11$, visualised over a spanwise distance of $z/D = 33$, in perspective and plan views, respectively, showing three wavelengths of this instability. Flow is from left to right in these images, with the cylinder rotating anticlockwise (a) G/D = 0.01, Re = 50, λ/D = 10 and (b) G/D = 0.22, Re = 80, λ/D = 15.

Fig. 12. (a) and (b) Visualisation of the spanwise perturbation vorticity contours for the mode C′ instability for the rotating cylinder at $\alpha = +1$ at the specified parameter values. Contour shading as per Fig. 4. (c) and (d) Three-dimensional reconstruction of this mode at $G/D = 0.3$, Re = 120, $\lambda/D = 2$, visualised over a spanwise distance of $z/D = 6$ in perspective and plan views, respectively, showing three wavelengths of this instability. Flow is from left to right in both images, with the cylinder rotating anticlockwise (a) G/D = 0.25, Re = 120, λ/D = 1.8 and (b) G/D = 0.35, Re = 135, λ/D = 1.8.

$\simeq 100$ as the gap height is increased, with a critical wavelength of $\simeq 2D$. The spatio-temporal characteristics of this mode are similar to those observed for a non-rotating cylinder, with the perturbations growing in the shear layers between the vortex being shed and the wall shear layer. Fig. 12(a) and (b) show spanwise perturbation vorticity contours of this mode at the specified parameter values, while Fig. 12(c) and (d) shows the three-dimensional reconstructions of this mode at $G/D = 0.3$, Re = 120 in perspective and plan views, respectively.

At higher Reynolds numbers, the two-dimensional wake becomes aperiodic for $G/D < 0.35$, thus preventing the three-dimensional stability to be characterised using standard linear stability analysis.

3.2.2.3. Mode A*. For $0.35 \leq G/D \leq 0.6$, the periodic two-dimensional base flow becomes unstable to a three-dimensional mode whose Floquet multiplier is real and positive. This mode has spatio-temporal characteristics similar to mode A and a similar spanwise wavelength ($\simeq 4D$). In order to simplify the nomenclature, this three-dimensional mode is named mode A*. The critical Reynolds number for the onset of this mode decreases as the gap height is increased to $G/D \simeq 0.4D$, and then increases as the gap height is increased. Shown in Fig. 13 are spanwise perturbation vorticity contours at specified gap heights and Reynolds numbers. Notice that unlike mode A, the perturbation field achieves the highest amplitudes far downstream where the wake has evolved to consists of a sequence of translating clockwise vortices formed from fluid passing over the top of the cylinder. Fig. 13(c) and (d) shows the three-dimensional reconstruction of this mode in perspective and plan views, respectively.

Shown in Fig. 14 are the perturbation contours of mode A* for increasing Reynolds numbers at $G/D = 0.6$, for a constant spanwise wavelength of $\lambda/D = 3.5$. While the perturbations grow in the far wake at lower Reynolds numbers, the perturbations move further upstream with increasing Reynolds number, eventually resembling mode A for a non-rotating cylinder. Previously, mode A transition has been postulated to be due to an elliptic instability of the vortex cores (Leweke and Williamson, 1998; Thompson et al., 2001). In addition, in the far wake, the perturbation spanwise vorticity signature in the cores is consistent with elliptic instability, which appears to be the reason that the perturbation grows as the vortices advect downstream, at least for the lower Reynolds number cases (see Fig. 13(b)).

3.2.2.4. Modes A and B. For the rotating cylinder in freestream, the onset of modes A and B is delayed to higher Reynolds numbers as the rotation rate is increased from $\alpha = 0$ to $\alpha = 1$ (Akoury et al., 2008; Rao et al., 2013a, 2015a). Here, for the forward rotating–translating cylinder, the onset of these modes is observed for larger gap heights, and for $G/D \gtrsim 2$, the critical values at onset asymptote to those observed for a rotating cylinder in freestream. Mode A is the first three-dimensional mode to be observed for $G/D \gtrsim 0.75$ and mode B is observed for $G/D \gtrsim 1$. The onset of mode B instability occurs at higher Reynolds numbers for smaller gap heights, with a corresponding decrease in the critical wavelength. Shown in Fig. 15 are the spanwise perturbation vorticity contours for modes A and B at the specified values.
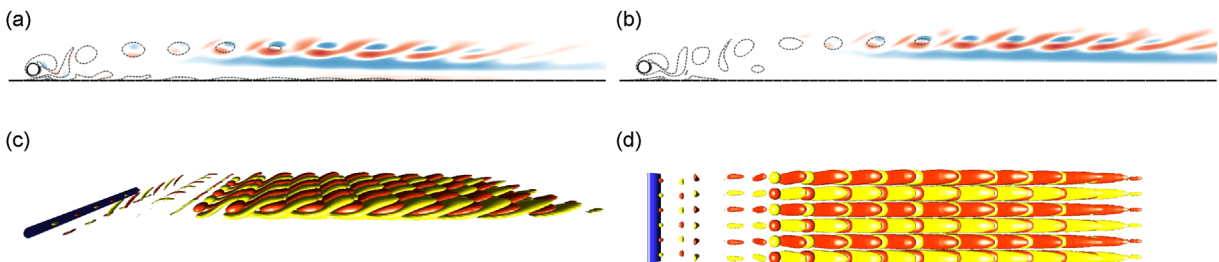

Fig. 13. (a) and (b) Visualisation of the spanwise perturbation vorticity contours for the mode A* instability for the rotating cylinder at $\alpha = +1$ at the specified parameter values. Contour shading as per Fig. 4. The wake is visualised for streamwise distances of $\gtrsim 45D$. (c) and (d) Three-dimensional reconstruction of this mode at $G/D = 0.6, \mathrm{Re} = 165, \lambda/D = 3.5$ over a spanwise distance of $z/D = 10.5$ in perspective and plan view, respectively, showing three wavelengths of this instability. Flow is from left to right in these images, with the cylinder rotating anticlockwise (a) $G/D = 0.4, \mathrm{Re} = 135, \lambda/D = 3.75$ and (b) $G/D = 0.6, \mathrm{Re} = 165, \lambda/D = 3.5$.
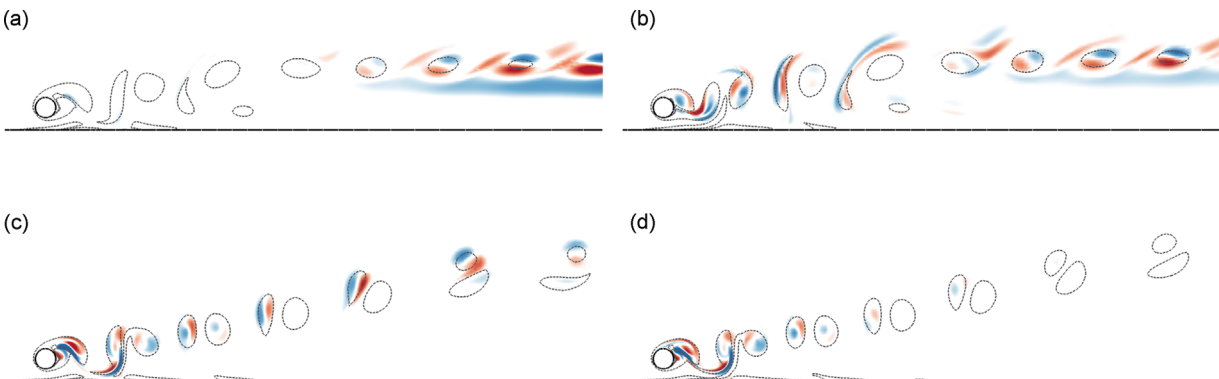

Fig. 14. Visualisation of the spanwise perturbation vorticity contours of mode A* for the cylinder rotating at $\alpha = +1$ for $G/D = 0.6, \lambda/D = 3.5$ at the specified Reynolds numbers. Contour shading as per Fig. 4. Flow is from left to right in all images, with the cylinder rotating anticlockwise (a) $\mathrm{Re} = 165$, (b) $\mathrm{Re} = 200$, (c) $\mathrm{Re} = 260$ and (d) $\mathrm{Re} = 300$.
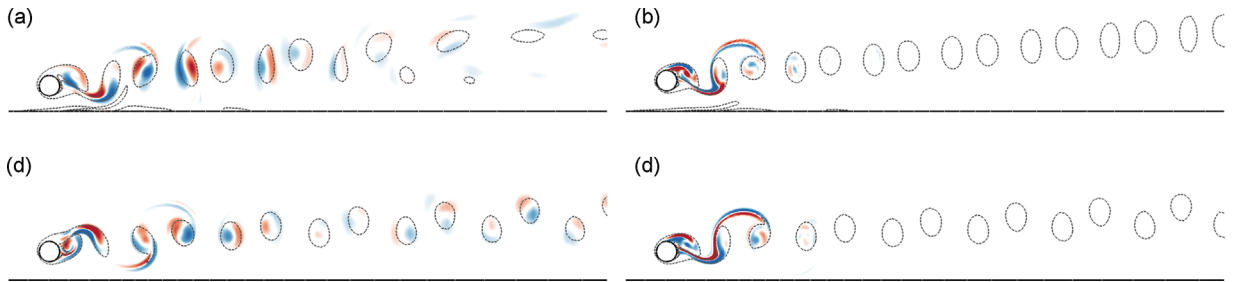
Fig. 15. Visualisation of the spanwise perturbation vorticity contours for the mode A and mode B instabilities for the rotating cylinder at $\alpha = +1$ at the specified parameter values. Contour shading as per Fig. 4. Flow is from left to right in all images, with the cylinder rotating anticlockwise (a) mode A: G/D = 0.75, Re = 180, λ/D = 3.5,(b) mode B: G/D = 1, Re = 360, λ/D = 0.77, (c) mode A: G/D = 5, Re = 280, λ/D = 3.75 and (d) mode B: G/D = 5, Re = 340, λ/D = 0.8.

Table 2
Summary of the modes showing the approximate characteristic wavelength, nature of the Floquet multiplier (μ), gap height at which the instability occurs and the base flow on which the mode occurs for the forward rolling cylinder ($\alpha = +1$) for Re $\leq$ 360.

Mode	λ/D	Base flow	Nature of μ	Gap height
A	$\simeq 4$	Unsteady	Periodic	$\gtrsim 0.75D - \infty$
A*	$\simeq 4$	Unsteady	Periodic	$\simeq 0.35D - 0.6D$
B	$\simeq 0.8$	Unsteady	Periodic	$\gtrsim 1D - \infty$
C'	$\simeq 2$	Unsteady	Subharmonic	$\simeq 0.25D - 0.35D$
E	$[8-14]$	Steady	Linear growth	$0 - 0.22D$

The characteristics of the three-dimensional modes observed in wake of a forward rolling cylinder for Re $\leq$ 360 are summarised in Table 2.

3.3. Translation plus reverse rolling: $\alpha = -1$

Fig. 16 shows the parameter space diagram for the reverse rolling cylinder at various heights from the wall for Re $\leq$ 400. Previous studies (Stewart et al., 2010; Rao et al., 2011) have shown that the onset of two- and three-dimensional flow are delayed to higher Reynolds numbers for a cylinder rolling along a wall. As the height of the cylinder above a wall increases, the onset of unsteady flow monotonically decreases from Re $\gtrsim$ 400 at G/D $\simeq$ 0 to Re $\simeq$ 50 at G/D $\gtrsim$ 5. Similar to the $\alpha = 0$ and +1 case, the first three-dimensional mode to become unstable on the steady flow for small gap heights is mode E, and for larger gap heights, (G/D $\simeq$ 0.4D), several new modes are observed. For 0.5 $\lesssim$ G/D $\lesssim$ 1, the flow remains two-dimensional for Re $\leq$ 400. For G/D $\simeq$ 1, modes A and B become unstable on the unsteady flow, with the critical Reynolds number for the onset of these modes decreasing from G/D $\simeq$ 1 to G/D = 5, where the values approach those seen in freestream (Rao et al., 2013a).

3.3.1. Two-dimensional flow

Fig. 17 shows the variation in the force coefficients with Reynolds numbers for the steady (subfigures (a) and (b)) and unsteady regimes (subfigures (c) and (d)). The filled symbols in these figures indicate that the flow is beyond the critical Reynolds number for three-dimensional transition. The force coefficients obey a power law relationship with Reynolds number in the steady regime, and are presented on a log–log plot. The variation of the time-averaged drag coefficient on the steady base flow takes the form $\overline{C_d} = a(\text{Re})^b(G/D)^c$; where, $a \simeq 15.60$, $b \simeq -0.712$ and $c \simeq -0.262$. The variation of the time-averaged lift coefficient on the steady base flow takes the form $\overline{C_l} = a(\text{Re})^b(G/D)^c$; where, $a \simeq 5$, $b \simeq -0.14$ and $c \simeq -0.11$. In the unsteady regime, the variation of the force coefficients with Reynolds numbers is fairly small for a given gap height.

Fig. 18 shows the variation in shedding frequencies with gap height for various Reynolds numbers. As with the $\alpha = 0$ case, St increases with Reynolds number.

3.3.2. Three-dimensional flow

3.3.2.1. Mode E. Similar to the $\alpha = 0$ and $\alpha = +1$ cases, mode E is the first mode to become unstable to three-dimensional perturbations on the steady base flow for small gap heights. The critical Reynolds number and the spanwise wavelength for three-dimensional transition both increase as the gap height is increased. The stability multiplier is real and positive. Shown in Fig. 19 are the spanwise perturbation vorticity contours at the specified gap heights. As the gap height increases, the length of the recirculation zone increases, essentially increasing the spatial region over which global instability can develop. As the Reynolds number is increased to higher values, the growth rate of mode E increases and the range of unstable spanwise wavelengths also increases.
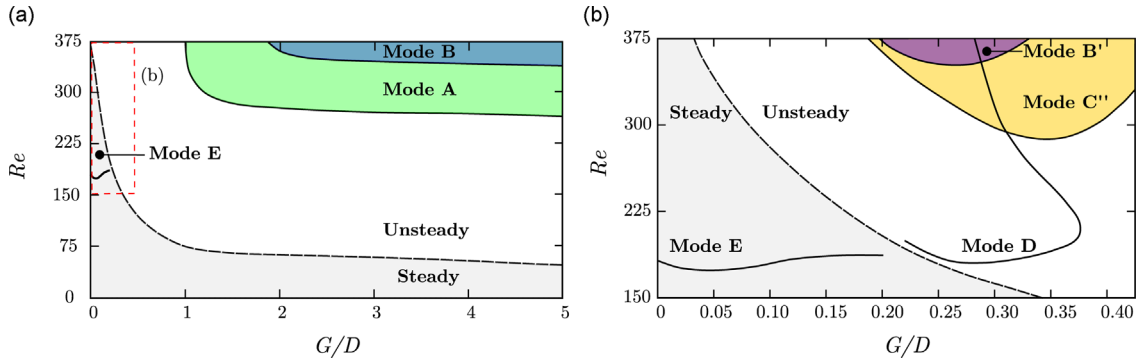
Fig. 16. (a) Parameter space for the cylinder rotating at $\alpha = -1$ showing the regimes of steady and unsteady flows and the existence of the various three-dimensional modes for $G/D \leq 5$, $Re \leq 375$. (b) Enlarged area of (a) showing the transitions that occur for $0 \leq G/D \lesssim 0.45$, $150 \leq Re \leq 375$. The steady regions of flow are shaded in grey and the dashed line (- -) indicates the approximate Reynolds number for the transition from steady to unsteady flow in both diagrams.
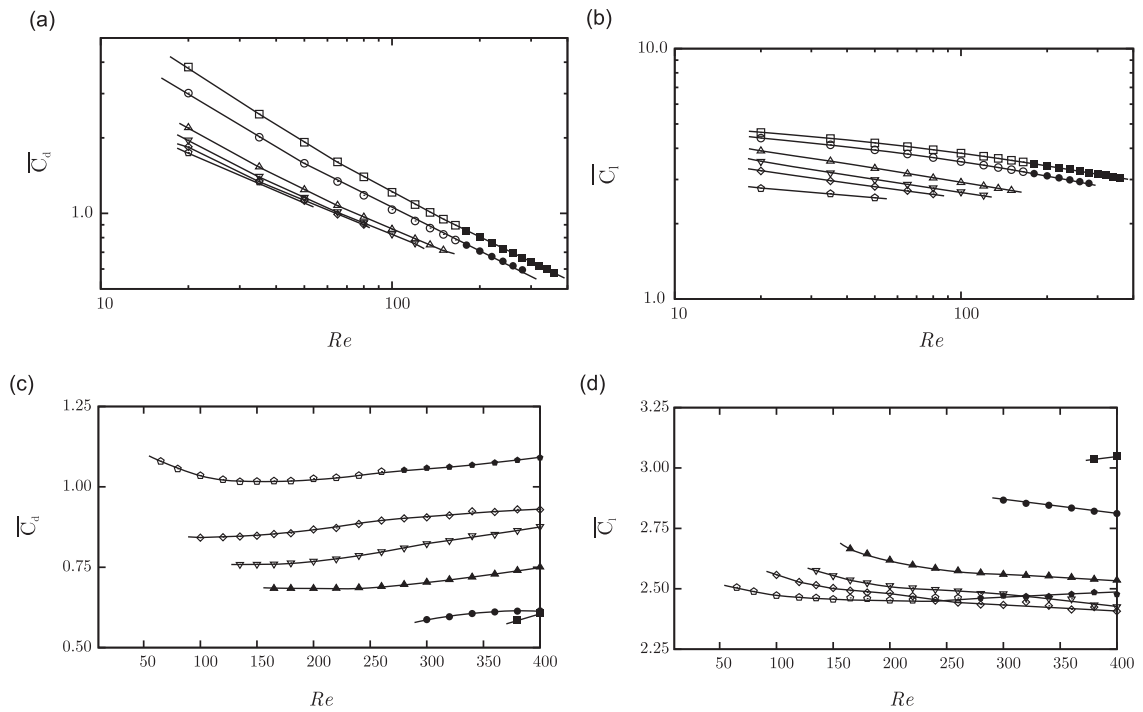

Fig. 17. (a) and (b) Variation of the time-averaged drag and lift coefficient (plotted on log–log scale) with Re for various gap heights for the cylinder translating with a rotation rate of $\alpha = -1$ in the steady regime $Re \leq 400$. (c) and (d) The variation of the time-averaged drag and lift coefficient in the unsteady regime. Open symbols indicate the flow is two-dimensional, while filled symbols indicate the flow is three-dimensional. Legend: square ($\square$, $\blacksquare$) - $G/D = 0.05$; circle ($\circ$, $\bullet$) - $G/D = 0.1$; upright triangle ($\triangle$, $\blacktriangle$) - $G/D = 0.3$; inverted triangle ($\triangledown$, $\blacktriangledown$) - $G/D = 0.5$; diamond ($\diamond$, $\blacklozenge$) - $G/D = 0.75$; pentagon ($\varhexagon$, $\pentagon$)- $G/D = 4$.
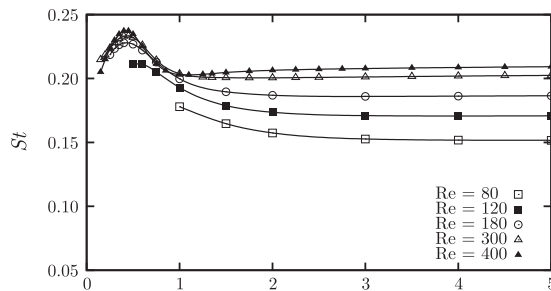

Fig. 18. Variation of St with G/D for the reverse rolling cylinder ($\alpha = -1$) at the specified Reynolds numbers.
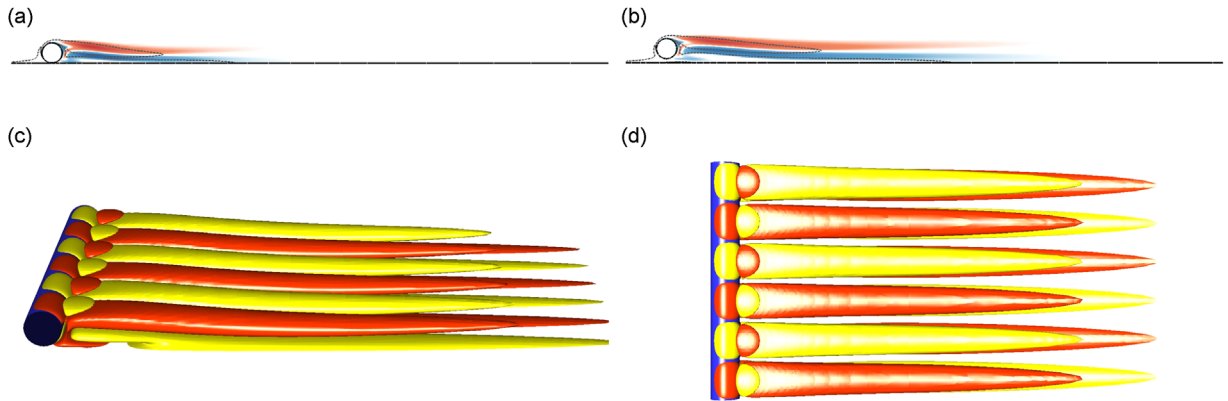
Fig. 19. (a) and (b) Visualisation of the spanwise perturbation vorticity contours for the mode E instability for the rotating cylinder at $\alpha = -1$ at the specified parameter values. Contour shading as per Fig. 4. (c) and (d) Three-dimensional reconstruction of this mode at $G/D = 0.2, \mathrm{Re} = 200, \lambda/D = 2.75$, visualised over a spanwise distance of $z/D = 8.25$ in perspective and plan views, respectively, showing three wavelengths of this instability. Flow is from left to right in these images, with the cylinder rotating clockwise (a) G/D = 0.01, Re = 180, λ/D = 2.2 and (b) G/D = 0.2, Re = 200, λ/D = 2.75.
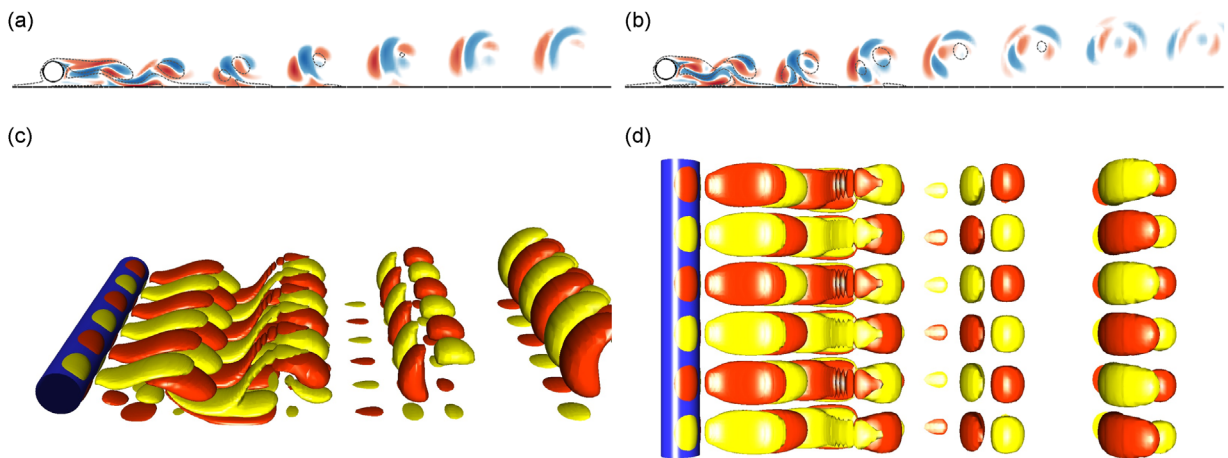

Fig. 20. (a) and (b) Visualisation of the spanwise perturbation vorticity contours for the Mode D instability for the rotating cylinder at $\alpha = -1$ at the specified parameter values. Contour shading as per Fig. 4. (c) and (d) Three-dimensional reconstruction of this mode at $G/D = 0.3, \mathrm{Re} = 200, \lambda/D = 2.6$, visualised over a spanwise distance of $z/D = 7.8$ in perspective and plan views, respectively, showing three wavelengths of this instability. Flow is from left to right in these images, with the cylinder rotating clockwise (a) G/D = 0.25, Re = 200, λ/D = 2.5 and (b) G/D = 0.37, Re = 220, λ/D = 2.2.

3.3.2.2. Mode D. For gap heights of $0.25 \leq G/D \leq 0.4$, the flow becomes unstable to a three-dimensional mode on the unsteady two-dimensional base flow. This mode has a spanwise wavelength similar to that of mode E instability ($\lambda_c/D \simeq 2.4$), with the Floquet multiplier being purely real and positive. This instability is termed Mode D, with nomenclature similar to that in Rao et al. (2013a, 2015a). Shown in Fig. 20(a) and (b) are the spanwise perturbation vorticity contours for this mode.

3.3.2.3. Mode C″. For gap heights of $0.22 \lesssim G/D \leq 0.45$, the flow becomes unstable to a subharmonic mode at higher Reynolds numbers. This mode has a real and negative Floquet multiplier and is named as mode C″. The average spanwise wavelength at onset of this mode is $\simeq 1.5D$. Shown in Fig. 21 are the spanwise perturbation vorticity contours at the specified gap heights. Fig. 21(d) and (e) shows the three-dimensional reconstruction of this mode in perspective and plan views, respectively.

3.3.2.4. Mode B′. For gap heights of $0.22 \lesssim G/D \leq 0.32$, the flow becomes unstable to a real mode at higher Reynolds numbers. This mode has a real and positive Floquet multiplier and is named as mode B′. The average spanwise wavelength at onset of this mode is $\simeq 0.8D$. Although the spanwise wavelength of this mode is similar to the mode B instability, the perturbations grow in the vortex cores and not in the braid shear layers. Shown in Fig. 22 are the spanwise perturbation vorticity contours at the specified gap heights. Fig. 22(d) and (e) shows the three-dimensional reconstruction of this mode in perspective and plan views, respectively.
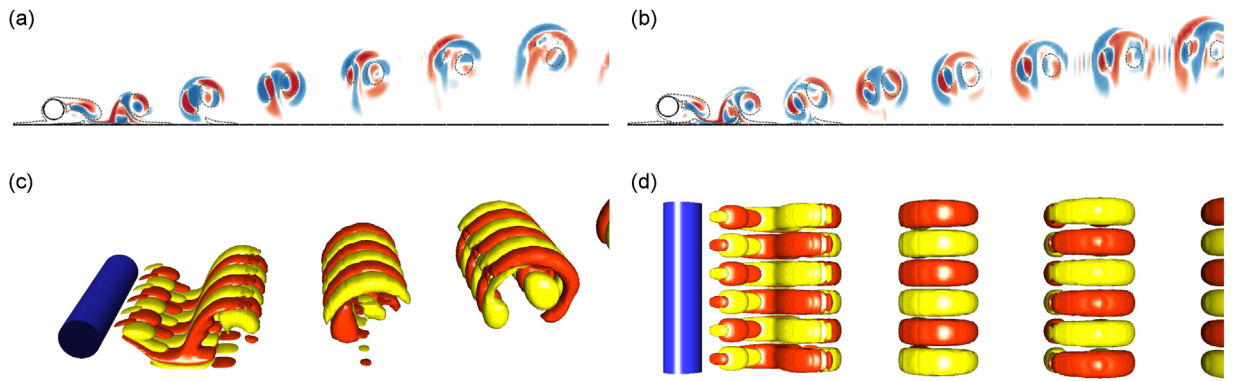
Fig. 21. (a) and (b) Visualisation of the spanwise perturbation vorticity contours for the Mode C″ instability for the rotating cylinder at $\alpha = -1$ at the specified parameter values. Contour shading as per Fig. 4. (c) and (d) Three-dimensional reconstruction of this mode at $G/D = 0.3$, $Re = 300$, $\lambda/D = 1.5$, visualised over a spanwise distance of $z/D = 4.5$ in perspective and plan views, respectively, showing three wavelengths of this instability. Flow is from left to right in these images, with the cylinder rotating clockwise (a) $G/D = 0.25$, $Re = 340$, $\lambda/D = 1.75$ and (b) $G/D = 0.4$, $Re = 320$, $\lambda/D = 1.4$.
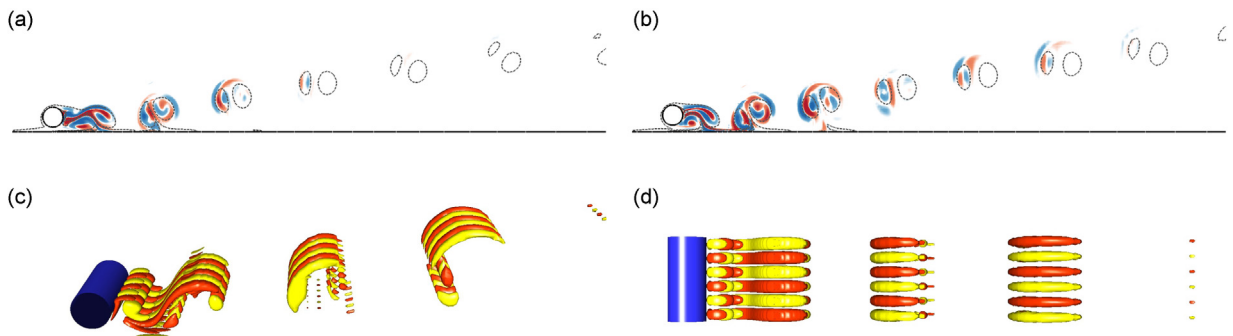

Fig. 22. (a) and (b) Visualisation of the spanwise perturbation vorticity contours for the mode B′ instability for the rotating cylinder at $\alpha = -1$ at the specified parameter values. Contour shading as per Fig. 4. (c) and (d) Three-dimensional reconstruction of this mode at $G/D = 0.3$, $Re = 360$, $\lambda/D = 0.75$, visualised over a spanwise distance of $z/D = 2.25$ in perspective and plan views, respectively, showing three wavelengths of this instability. Flow is from left to right in these images, with the cylinder rotating clockwise (a) $G/D = 0.22$, $Re = 380$, $\lambda/D = 0.85$ and (b) $G/D = 0.32$, $Re = 380$, $\lambda/D = 0.75$.
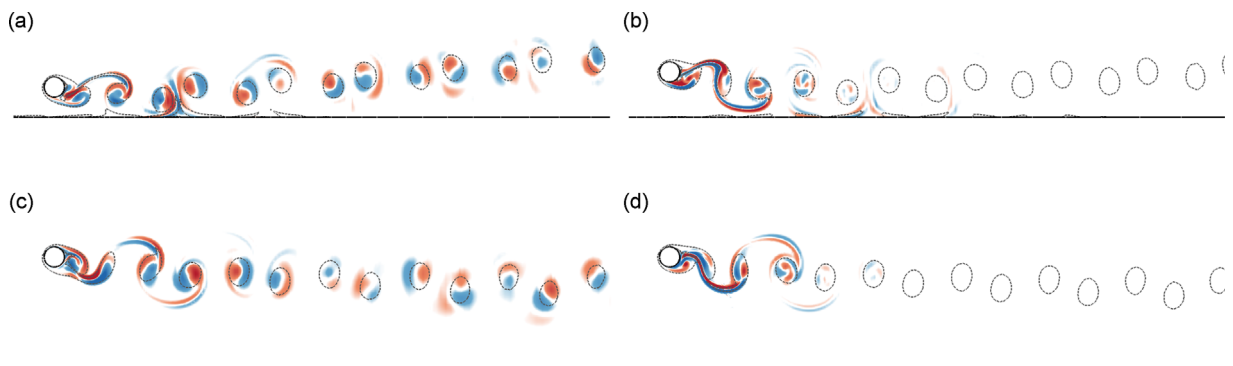

Fig. 23. Visualisation of the spanwise perturbation vorticity contours for the mode A and mode B instabilities for the rotating cylinder at $\alpha = -1$ at the specified parameter values. Contour shading as per Fig. 4. Flow is from left to right in all images, with the cylinder rotating clockwise (a) mode A: $G/D = 1$, $Re = 380$, $\lambda/D = 3.4$, (b) mode B: $G/D = 1.75$, $Re = 380$, $\lambda/D = 0.75$, (c) mode A: $G/D = 5$, $Re = 280$, $\lambda/D = 3.75$ and (d) mode B: $G/D = 5$, $Re = 350$, $\lambda/D = 0.8$.

3.3.2.5. Mode A and B. Modes A and B first become unstable for larger gap heights of $G/D \simeq 1$. The critical Reynolds numbers for the onset of modes A and B decrease with an increase in gap height, and asymptote to the values corresponding to an isolated non-rotating cylinder. As with the isolated non-rotating cylinder, onset of mode A occurs prior to the onset of mode B. Fig. 23 shows spanwise perturbation vorticity contours at the specified parametric values. The Floquet multipliers of both these modes are real and positive. The critical spanwise wavelength of the mode A instability at onset increases as the gap height is increased from $\lambda_c/D \simeq 3.4$ at $G/D = 1$ to $\lambda_c/D \simeq 3.9$ at $G/D = 5$, while that of mode B remains $\simeq 0.8D$ over the entire range.

The characteristics of the three-dimensional modes observed in wake of a reverse rolling cylinder for Re ≤ 400 are summarised in Table 3.

4. Behaviour of the mode E instability at greater gap heights

Recent studies by Rao et al. (2015a) showed that mode E was the first three-dimensional mode to become unstable for a non-rotating cylinder on an artificially stabilised two-dimensional base flow. While the critical Reynolds number for the onset of this mode increased as the rotation rate was increased (Figs. 2, 7 and 16(a)), this mode is not physically realisable. This is because it develops on base flows at Reynolds numbers beyond transition to BvK shedding at Re ≃ 47. For the cases examined in this paper, mode E is the first three-dimensional mode to become unstable to perturbations, irrespective of the rotation rate for $G/D{\lesssim}0.25$. In this section, for $0.25 \leq G/D \leq 5$, mode E transition is predicted for steady base flows beyond the critical Reynolds number for the onset of shedding for the three-rotation rates. Linear stability analysis is carried out on the stabilised base flows and the growth rate of the three-dimensional modes are monitored. Fig. 24 shows the variation of the critical Reynolds number for the mode E transition for the three rotation rates investigated. The critical Reynolds numbers increase with gap height up to $G/D \simeq 0.3$, and at greater gap heights the critical values for transition approaches those observed by Rao et al. (2015a). Fig. 25 shows spanwise perturbation vorticity contours of mode E as a function of gap height for the non-rotating cylinder. These figures indicate that the structure of the perturbation does not change significantly with the increase in gap height as the top recirculation zone decreases in length as the gap height is increased.

Fig. 26(a) and (b) shows the perturbation vorticity contours for mode E instability for the cylinder translating at $G/D = 5$ with rotation rates of $\alpha = +1$ and -1, respectively. The perturbation fields appear to be flipped vertically due to the forward and reverse rotations imposed on the cylinder surface, but are nonetheless identical to the mode E structure for an isolated rotating cylinder (also see Fig. 6(c) of Rao et al. (2015a)).

5. Conclusions

A systematic study of rotating cylinders translating parallel to a wall was undertaken, quantifying the transition of three-dimensional flow as a function of gap height. For each of the three rotation rates studied, parameter maps showing neutral stability boundaries and the regions of existence of the three-dimensional modes were presented. For the non-rotating translating cylinder, two new modes become unstable for $G/D \leq 0.4$, both of which are subharmonic. Mode C′ appears to be associated with the stretched shear layers in the near wake, while mode C* grows in the far wake. At higher Reynolds numbers, mode B was found to become unstable to three-dimensional perturbations, as in the case of an isolated cylinder (Barkley and Henderson, 1996; Williamson, 1988). However, the onset of mode B is delayed to higher Reynolds numbers at lower gap heights ($G/D \simeq 1$). Since the presence of the wall removes the centreline wake spatio-temporal symmetry, and

Table 3
Summary of the modes showing the approximate characteristic wavelength, nature of the Floquet multiplier (μ), gap height at which the instability occurs and the base flow on which the mode occurs for the reverse rolling cylinder ($\alpha = -1$) for Re ≤ 400.

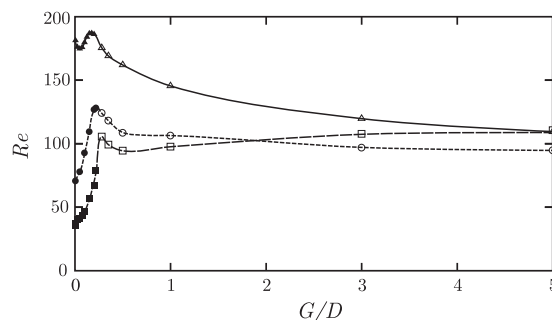| Mode	λ/D	Base flow	Nature of μ	Gap height
A	$\simeq 4$	Unsteady	Periodic	$\gtrsim 1D–\infty$
B	$\simeq 0.8$	Unsteady	Periodic	$\gtrsim 1.75D–\infty$
B′	$\simeq 0.77$	Unsteady	Periodic	$\simeq 0.22D–0.32D$
C″	$\simeq 1.5$	Unsteady	Subharmonic	$\gtrsim 0.22D–0.45D$
D	$\simeq 2.4$	Unsteady	Periodic	$\simeq 0.22D–0.37D$
E	$\simeq 2.4$	Steady	Linear growth	$0–0.2D$

Fig. 24. Variation of the mode E instability with gap height for the three rotation rates. Filled symbols indicate values of critical Reynolds number on the steady state, while open symbols indicate values on the stabilised base flow. Legend: $\alpha = 0$ - circles (●, ○); $\alpha = +1$ - squares (■, □); $\alpha = -1$ - triangles (△, ▲).

(a)   (b)

(c)   (d)
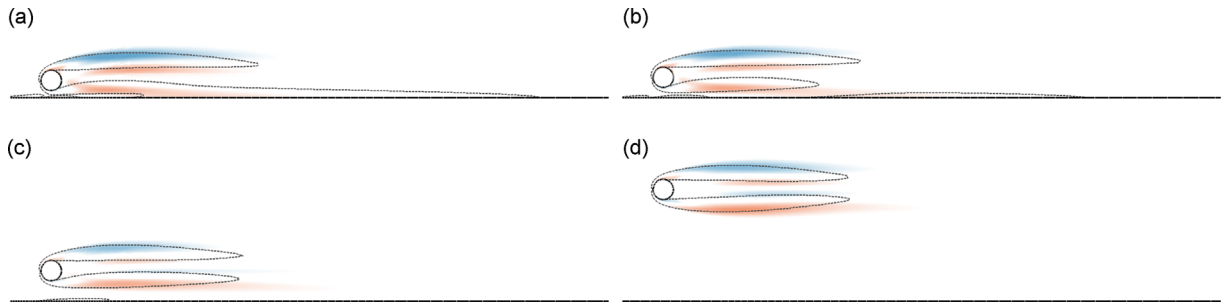
Fig. 25. Visualisation of the spanwise perturbation vorticity contours for the non-rotating cylinder at the specified gap heights at $Re = 120, \lambda/D = 5$ showing the mode E instability on the stabilised base flows. Contour shading as per Fig. 4. Flow is from left to right in all images (a) G/D = 0.35, (b) G/D = 0.5, (c) G/D = 1 and (d) G/D = 5.

(a)   (b)
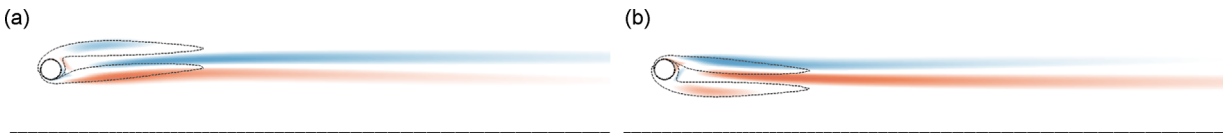
Fig. 26. Visualisation of the spanwise perturbation vorticity contours at $G/D = 5, Re = 120, \lambda/D = 5$ for (a) $\alpha = +1$ and (b) $\alpha = -1$. Contour shading as per Fig. 4. Flow is from left to right in all images (a) α = +1 and α = −1.

suppresses the absolute wake instability for BvK shedding at small gap heights, large modifications to the transition scenarios should not be surprising.

For a positive rotation rate of $\alpha = +1$, the transition scenario is similar, with the onset of the mode E instability on the steady flow, followed by the transition to the high growth rate subharmonic three-dimensional mode, mode C′ for $0.25 \lesssim G/D \lesssim 0.35$. At slightly greater gap heights, a real three-dimensional mode, mode A*, which grows in the far wake, is found to become unstable. Its neutral stability curve smoothly merges with that for mode A at higher Reynolds numbers. Both modes A and A* share the share spatio-temporal symmetries. Thus, these modes appear to be different manifestations of the same mode, but show high amplitude in different parts of the wake. The critical Reynolds number for mode A transition increases monotonically from $Re_c \simeq 175$ at $G/D \simeq 0.75$ to $Re_c \simeq 270$ for $G/D \gtrsim 5$. The neutral stability curve for mode B shows similar behaviour to that for the $\alpha = 0$ case, where the transition values increase as the gap height is decreased.

For a negative rotation rate of $\alpha = -1$, the critical Reynolds number for the transition to two-dimensional unsteady flow decreases monotonically from $Re \simeq 420$ at $G/D \simeq 0$ to $Re \simeq 50$ for $G/D \gtrsim 5$. Once again, on the steady flow, mode E is the first three-dimensional mode to become unstable. The critical Reynolds number for the onset of mode E is much higher than for $\alpha = 0$ and $\alpha = 1$, and occurs at a much shorter spanwise wavelength. As the gap height is increased, two real modes and one subharmonic mode are observed on the unsteady base flow for $G/D \lesssim 0.45$ and $Re \leq 375$, while the flow remains two-dimensional for $0.45 \lesssim G/D \lesssim 1$ and $Re \leq 375$. For $G/D \gtrsim 1$, modes A and B become unstable, with the critical Reynolds numbers for transition asymptoting to those observed in the flow past a rotating cylinder in freestream at large gap heights (Akoury et al., 2008; Rao et al., 2013a).

An extensive parameter space has been mapped here for a rotating cylinder translating near a wall for $Re \leq 400$, with several new three-dimensional transition identified. The existence regions of these modes in the Re–G/D parameter space have been presented, along with the visualisations of the perturbation fields. At the upper limit of the Reynolds number range for the linear stability analysis, it is probable that the quasi-periodic mode predicted for a non-rotating cylinder, mode QP, may become marginally unstable for $\alpha = +1$ and -1; this was not explored further as the growth rates of mode A and mode B were significantly higher.

Acknowledgements

References

Akoury, R.E., Braza, M., Perrin, R., Harran, G., Hoarau, Y., 2008. The three-dimensional transition in the flow around a rotating cylinder. Journal of Fluid Mechanics 607, 1–11.

Barkley, D., Henderson, R.D., 1996. Three-dimensional Floquet stability analysis of the wake of a circular cylinder. Journal of Fluid Mechanics 322, 215–241.

Blackburn, H.M., Lopez, J.M., 2003. On three-dimensional quasiperiodic Floquet instabilities of two-dimensional bluff body wakes. Physics of Fluids 15, L57–L60.

Blackburn, H.M., Marques, F., Lopez, J.M., 2005. Symmetry breaking in two-dimensional time-periodic wakes. Journal of Fluid Mechanics 552, 395–411.

Cheng, M., Luo, L.S., 2007. Characteristics of two-dimensional flow around a rotating circular cylinder near a plane wall. Physics of Fluids 19, 063601.

Gupta, P., Ismadi, M.Z., Verma, P., Fouras, A., Jadhav, S., Bellare, J., Hourigan, K., 2014. Optimization of agitation speed in spinner flask for microcarrier structural integrity and expansion of induced pluripotent stem cells. Cytotechnology 26 (July) (2014), 1–15.

Henderson, R.D., 1997. Nonlinear dynamics and pattern formation in turbulent wake transition. Journal of Fluid Mechanics 352, 65–112.

Hourigan, K., Rao, A., Brøns, M., Leweke, T., Thompson, M.C., 2013. Vorticity generation and wake transition for a translating circular cylinder: wall proximity and rotation effects. Journal of Wind Engineering and Industrial Aerodynamics 122, 2–9.

Huang, W.X., Sung, H.J., 2007. Vortex shedding from a circular cylinder near a moving wall. Journal of Fluids and Structures 23, 1064–1076.

Ismadi, M.Z., Hourigan, K., Fouras, A., 2014. Experimental characterisation of fluid mechanics in a spinner flask bioreactor. Processes 2, 753–772.

Kang, S., Choi, H., Lee, S., 1999. Laminar flow past a rotating circular cylinder. Physics of Fluids 11, 3312–3321.

Karniadakis, G.E., Sherwin, S.J., 2005. Spectral/hp Methods for Computational Fluid Dynamics. Oxford University Press, Oxford.

Leontini, J.S., Lo Jacono, D., Thompson, M.C., 2013. Wake states and frequency selection of a streamwise oscillating cylinder. Journal of Fluid Mechanics 730, 162–192.

Leontini, J.S., Thompson, M.C., Hourigan, K., 2007. Three-dimensional transition in the wake of a transversely oscillating cylinder. Journal of Fluid Mechanics 577, 79–104.

Leweke, T., Williamson, C.H.K., 1998. Cooperative elliptic instability of a vortex pair. Journal of Fluid Mechanics 360, 85–119.

Mittal, S., Kumar, B., 2003. Flow past a rotating cylinder. Journal of Fluid Mechanics 476, 303–334.

Pralits, J.O., Brandt, L., Giannetti, F., 2010. Instability and sensitivity of the flow around a rotating circular cylinder. Journal of Fluid Mechanics 650, 513–536.

Radi, A., Thompson, M.C., Rao, A., Hourigan, K., Sheridan, J., 2013. Experimental evidence of new three-dimensional modes in the wake of a rotating cylinder. Journal of Fluid Mechanics 734, 567–594.

Rao, A., Leontini, J., Thompson, M.C., Hourigan, K., 2013a. Three-dimensionality in the wake of a rotating cylinder in a uniform flow. Journal of Fluid Mechanics 717, 1–29.

Rao, A., Leontini, J.S., Thompson, M.C., Hourigan, K., 2013b. Three-dimensionality in the wake of a rapidly rotating cylinder in uniform flow. Journal of Fluid Mechanics 730, 379–391.

Rao, A., Passaggia, P.Y., Bolnot, H., Thompson, M.C., Leweke, T., Hourigan, K., 2012. Transition to chaos in the wake of a rolling sphere. Journal of Fluid Mechanics 695, 135–148.

Rao, A., Radi, A., Leontini, J.S., Thompson, M.C., Sheridan, J., Hourigan, K., 2015a. A review of rotating cylinder wake transitions. Journal of Fluids and Structures 53, 2–14.

Rao, A., Radi, A., Leontini, J.S., Thompson, M.C., Sheridan, J., Hourigan, K., 2015b. The influence of a small upstream wire on transition in a rotating cylinder wake. Journal of Fluid Mechanics, 769. available online.

Rao, A., Stewart, B.E., Thompson, M.C., Leweke, T., Hourigan, K., 2011. Flows past rotating cylinders next to a wall. Journal of Fluids and Structures 27, 668–679.

Rao, A., Thompson, M.C., Leweke, T., Hourigan, K., 2013c. Dynamics and stability of the wake behind tandem cylinders sliding along a wall. Journal of Fluid Mechanics 722, 291–316.

Rao, A., Thompson, M.C., Leweke, T., Hourigan, K., 2013d. The flow past a circular cylinder translating at different heights above a wall. Journal of Fluids and Structures 41, 9–21. Special issue on Bluff Body Flows (Blubof2011).

Robichaux, J., Balachandar, S., Vanka, S.P., 1999. Three-dimensional Floquet instability of the wake of a square cylinder. Physics of Fluids 11, 560–578.

Russel, W.B., Hinch, E.J., Leal, L.G., Tieffenbruck, G., 1977. Rods falling near a vertical wall. Journal of Fluid Mechanics 83, 273–287.

Ryan, K., Thompson, M.C., Hourigan, K., 2005. Three-dimensional transition in the wake of bluff elongated cylinders. Journal of Fluid Mechanics 538, 1–29.

Sheard, G.J., 2011. Wake stability features behind a square cylinder: focus on small incidence angles. Journal of Fluids and Structures 27, 734–742.

Sheard, G.J., Fitzgerald, M.J., Ryan, K., 2009. Cylinders with square cross-section: wake instabilities with incidence angle variation. Journal of Fluid Mechanics 630, 43–69.

Sheard, G.J., Thompson, M.C., Hourigan, K., 2004a. Asymmetric structure and non-linear transition behaviour of the wakes of toroidal bodies. European Journal of Mechanics B—Fluids 23, 167–179. Bluff Body Wakes and Vortex-Induced Vibrations.

Sheard, G.J., Thompson, M.C., Hourigan, K., 2004b. From spheres to circular cylinders: non-axisymmetric transitions in the flow past rings. Journal of Fluid Mechanics 506, 45–78.

Sheard, G.J., Thompson, M.C., Hourigan, K., 2005a. Subharmonic mechanism of the mode C instability. Physics of Fluids 17, 1–4.

Sheard, G.J., Thompson, M.C., Hourigan, K., Leweke, T., 2005b. The evolution of a subharmonic mode in a vortex street. Journal of Fluid Mechanics 534, 23–38.

Stewart, B.E., Hourigan, K., Thompson, M.C., Leweke, T., 2006. Flow dynamics and forces associated with a cylinder rolling along a wall. Physics of Fluids 18, 1117011–1117014.

Stewart, B.E., Thompson, M.C., Leweke, T., Hourigan, K., 2010. The wake behind a cylinder rolling on a wall at varying rotation rates. Journal of Fluid Mechanics 648, 225–256.

Stojković, D., Breuer, M., Durst, F., 2002. Effect of high rotation rates on the laminar flow around a circular cylinder. Physics of Fluids 14, 3160–3178.

Stojković, D., Schön, P., Breuer, M., Durst, F., 2003. On the new vortex shedding mode past a rotating circular cylinder. Physics of Fluids 15, 1257–1260.

Taneda, S., 1965. Experimental investigation of vortex streets. Journal of the Physical Society of Japan 20, 1714–1721.

Thompson, M.C., Hourigan, K., Cheung, A., Leweke, T., 2006a. Hydrodynamics of a particle impact on a wall. Applied Mathematical Modelling 30, 1356–1369.

Thompson, M.C., Hourigan, K., Ryan, K., Sheard, G.J., 2006b. Wake transition of two-dimensional cylinders and axisymmetric bluff bodies. Journal of Fluids and Structures 22, 793–806.

Thompson, M.C., Hourigan, K., Sheridan, J., 1996. Three-dimensional instabilities in the wake of a circular cylinder. Experimental Thermal and Fluid Science 12, 190–196.

Thompson, M.C., Leweke, T., Williamson, C.H.K., 2001. The physical mechanism of transition in bluff body wakes. Journal of Fluids and Structures 15, 607–616.

Thompson, M.C., Radi, A., Rao, A., Sheridan, J., Hourigan, K., 2014. Low-Reynolds-number wakes of elliptical cylinders: from the circular cylinder to the normal flat plate. Journal of Fluid Mechanics 751, 570–600.

Williamson, C.H.K., 1988. The existence of two stages in the transition to three-dimensionality of a cylinder wake. Physics of Fluids 31, 3165–3168.

Williamson, C.H.K., 1996a. Three-dimensional vortex dynamics in bluff body wakes. Experimental Thermal and Fluid Science 12, 150–168.

Williamson, C.H.K., 1996b. Vortex dynamics in the cylinder wake. Annual Review of Fluid Mechanics 28, 477–539.

Yildirim, I., Rindt, C.C.M., van Steenhoven, A.A., 2013. Mode C flow transition behind a circular cylinder with a near-wake wire disturbance. Journal of Fluid Mechanics 727, 30–55.

Yoon, H., Lee, J., Chun, H., 2007. A numerical study on the fluid flow and heat transfer around a circular cylinder near a moving wall. International Journal of Heat and Mass Transfer 50, 3507–3520.

Yoon, H., Lee, J., Seo, J., Park, H., 2010. Characteristics for flow and heat transfer around a circular cylinder near a moving wall in wide range of low Reynolds number. International Journal of Heat and Mass Transfer 53, 5111–5120.

Zhang, X., Mohan, S., Van Den-Berg, M., Williams, C., 2005. Aerodynamics of a half-cylinder in ground effect. In: Engineering Turbulence Modelling and Experiments 6: ERCOFTAC International Symposium on Engineering Turbulence and Measurements - ETMM6. Elsevier Science B.V., pp. 461–470.